nature photonics

Article

https://doi.org/10.1038/s41566-023-01326-6

Wavelength-accurate nonlinear conversion through wavenumber selectivity in photonic crystal resonators

Received: 20 November 2022

Accepted: 3 October 2023

Published online: 16 November 2023

Check for updates

Jordan R. Stone [1,2] ✉, Xiyuan Lu [1,2], Gregory Moille [1,2], Daron Westly [2], Tahmid Rahman [1,2] & Kartik Srinivasan [1,2] ✉

Integrated nonlinear wavelength converters transfer optical energy from lasers or quantum emitters to other useful colours, but chromatic dispersion limits the range of achievable wavelength shifts. Moreover, because of geometric dispersion, fabrication tolerances reduce the accuracy with which devices produce specific target wavelengths. Here we report nonlinear wavelength converters that allow output wavelengths to be controlled with high accuracy despite their operation not being contingent on dispersion engineering. In our scheme, coupling between counterpropagating waves in a photonic crystal microresonator induces a photonic bandgap that isolates (in dispersion space) specific wavenumbers for nonlinear gain. We demonstrate the wide applicability of this strategy by simulating its use in third-harmonic generation, Kerr-microcomb dispersive wave formation and four-wave mixing Bragg scattering. In experiments, we demonstrate Kerr optical parametric oscillators in which such wavenumber-selective coupling designates the signal mode. As a result, differences between the targeted and realized signal wavelengths are <0.3%. Moreover, leveraging the bandgap-protected wavenumber selectivity, we continuously tune the output frequencies by nearly 300 GHz without compromising efficiency. Our results will bring about a paradigm shift in how microresonators are designed for nonlinear optics, and they make headway on the larger problem of building wavelength-accurate light sources using integrated photonics.

Controlling integrated microsystems to generate light with properties that are specifically geared to applications is a fundamental ambition of photonics research. For example, optical atomic clocks require ultra-coherent laser light with wavelengths precisely matched to atomic transitions, and future hybrid quantum networks will interface sources of non-classical light (for example, single photons) tuned to qubit wavelengths[1–4]. A powerful tool to meet the demands of such systems is optical nonlinearity, which can mould light on a quantum level and stimulate wavelength conversion (for example, through four-wave mixing (FWM)) for spectral access beyond conventional laser gain. In particular, optical microresonators with Kerr ($\chi^{(3)}$) nonlinearity have, after multiple groundbreaking demonstrations, become a linchpin of nonlinear photonics. They support microcombs for frequency synthesis, timekeeping and sensing[5–8]; optical parametric oscillators (μOPOs) for wavelength-flexible sources of laser light[9–11], squeezed light[12,13] and entangled photon pairs[14,15]; four-wave mixing Bragg

[1]Joint Quantum Institute, NIST/University of Maryland, College Park, MD, USA. [2]National Institute for Standards and Technology, Gaithersburg, MD, USA. ✉e-mail: jordan.stone@nist.gov; kartik.srinivasan@nist.gov

scattering (FWM-BS) for spectral translation of single photons[16]; third-harmonic generation (THG)[17,18]; and more. Although appreciable efficiencies have been shown in some cases, it remains a challenge to ensure a priori (that is, before testing) that a specific device will achieve the desired combination of wavelength accuracy and efficiency.

To elucidate the problem, we recall some basic design considerations for Kerr-nonlinear microresonators, focusing on commonly used microring devices. Fundamentally, energy and momentum conservation regulate FWM[19]; therefore, to within (approximately) a resonator linewidth, a set of resonator modes should obey:

$$\sum_i \nu_i = \sum_j \nu_j, \tag{1}$$

$$\sum_i m_i = \sum_j m_j, \tag{2}$$

where m_i is the azimuthal number (fundamentally related to the wavenumber) associated with a resonator mode with frequency ν_i, and the left-hand (right-hand) terms denote photons created (annihilated) during the FWM process. The pair of equations (1) and (2) is exact when ν_i and m_i refer to field quantities. In general, group velocity dispersion (GVD) induces a frequency mismatch, such that a set of modes satisfying equation (2) does not simultaneously satisfy equation (1). The strategic 'dispersion engineering' of modes to satisfy both equations (1) and (2) is ubiquitous in guided-wave nonlinear photonics, with the most popular approach being to complement material dispersion with dispersion arising from the microresonator geometry[20–22]. However, modelling broadband spectra, such as octave-spanning microcombs or μOPOs with widely separated wavelengths, often requires retaining six or more orders in a Taylor expansion of $\nu_i(m_i)$ around the pump wavelength[23,24]. In this regime, the mode wavelengths that satisfy both equations (1) and (2) are extremely sensitive to geometry. Hence, small errors in the device geometry (arising from either fabrication uncertainties or incomplete modelling) can amount to substantial differences between the simulated and experimentally observed spectrum. This necessitates the fabrication of many (often, hundreds or more) devices with nanometre-scale parameter variations. Ultimately, one negotiates a trade-off between the number of devices that require testing and the dispersion tolerance of a given application. In many cases, a simple geometry-based solution to realize a particular GVD (for example, one based on controlling the dimensions of a waveguide) does not exist. To make matters worse, unwanted nonlinear couplings (for example, Raman scattering, mode competition, and so on) can compete with or even suppress the targeted process[16,25–27].

Here we demonstrate Kerr-nonlinear wavelength conversion for which the m values of participating resonator modes are guaranteed from design; however, our method actually alleviates design constraints, naturally suppresses unwanted nonlinear couplings and does not rely on the sensitive control of higher-order GVD. We show how wavenumber-selective coherent coupling (hereafter referred to simply as 'coherent coupling') between counterpropagating waves in a photonic crystal microresonator induces controlled frequency splittings that balance the underlying GVD to satisfy both equations (1) and (2). We analyse optical parametric oscillation (OPO), THG, dispersive wave enhancement (DWE) in microcombs and FWM-BS by introducing coherent coupling into simulations of those systems, and we prove our ideas experimentally using the flexible example of μOPOs. Through the photonic crystal grating period, we dictate m values for the signal modes in three different μOPOs, and we showcase their tolerance to higher-order GVD by reproducing the same signal wavelength when pumping four separate modes of a single device. The generated signal wavelengths agree with simulations to within 0.3%. We characterize the μOPOs by their threshold power and conversion efficiency, and we find that our measurements agree with a model based on the Lugiato–Lefever equation (LLE). Finally, we highlight the protected nature of our method by tuning the μOPO output frequencies continuously over 300 GHz without sacrificing efficiency or inducing mode hopping. Our work re-envisions the design process for nonlinear wavelength converters, enables nonlinear optics in new spectral regions and with strongly dispersive materials and invites fundamental studies of nonlinear physics in photonic crystal microresonators.

Photonic crystal-mediated FWM

Figure 1 depicts a photonic crystal microresonator and illustrates the four FWM processes we study. For concreteness, we consider silicon nitride (SiN (that is, Si_3N_4)) microrings where the ring width, RW′, varies along the inner boundary according to $RW' = RW + A_{mod}\cos(N\theta)$, where RW is the nominal ring width, A_{mod} is the photonic crystal grating modulation amplitude, N is the photonic crystal grating period (an integer) and θ is the resonator azimuthal angle. Therefore, the spatial period of modulation is $2\pi R/N$, where R is the ring radius. The modulation creates a refractive index grating that coherently couples clockwise (CW) and counterclockwise (CCW) travelling-wave modes with the azimuthal number $m = N/2$, where m is an integer related to the wavenumber k via $k = m/R$. Hence, we say that the coherent coupling is 'wavenumber-selective'. The coupling rate, J, is proportional to A_{mod} and corresponds to half the frequency splitting between two supermodes, denoted '+' and '−' for the higher- and lower-frequency resonances, respectively (as pictured in the centre of Fig. 1). This type of resonator has numerous functionalities, including for sensing[28,29] and the slowing of light[30]. In the context of nonlinear optics, pump mode hybridization has been used to induce spontaneous pulse formation and facilitate parametric oscillations in resonators with normal GVD[31–33]. Moreover, modulations with different N values can be combined to realize multi-wavelength dispersion engineering[34–36]. In these experiments and others, J could be made larger than the resonator free spectral range (FSR) without reducing the quality factor.

In our experiments, we focus on μOPOs, which generate monochromatic signal and idler waves from a continuous-wave pump laser through resonantly enhanced degenerate FWM, as shown at the top (energy diagram and optical spectrum) of Fig. 1. Momentum conservation requires $2m_p = m_s + m_i$, where m_p, m_s and m_i are azimuthal numbers for the pump, signal and idler modes, respectively. Hence, mode pairs with $m = m_p \pm \mu$, where μ is an integer, may support μOPO if their resonance frequencies obey equation (1). In general, GVD prevents such frequency matching; that is, the associated FWM process does not conserve energy. In Fig. 1, the grey dashed lines in the energy diagrams and optical spectra illustrate how GVD suppresses FWM. To quantify this concept, we define the frequency mismatch as:

$$\Delta\nu = \nu_\mu + \nu_{-\mu} - 2\nu_0, \tag{3}$$

where ν_0 is the pump mode frequency and ν_μ is the mode frequency associated with the azimuthal number $m_p + \mu$. Normal GVD gives $\Delta\nu < 0$ for all μ and thus prevents FWM. Nonetheless, applying an appropriate shift to ν_μ (or $\nu_{-\mu}$) will restore energy conservation and activate the μOPO, as illustrated by the blue lines in Fig. 1. We can realize this shift via the '+' supermode; changing to the '+' basis gives the transformation:

$$\Delta\nu_+ = \begin{cases} \Delta\nu_{CW} + J, & m = \{N/2, 2m_p - N/2\} \\ \Delta\nu_{CW}, & \text{else} \end{cases} \tag{4}$$

where $\Delta\nu_{CW}$ is the frequency mismatch in the CW basis. Hence, we select m_s by choosing $N = 2m_s$, and the μOPO is activated when $J = -\Delta\nu_{CW}$. Note that, from equation (3), $\Delta\nu_+(\mu) = \Delta\nu_+(-\mu)$; hence, the mismatch is shifted for both signal and idler modes. In Supplementary Fig. 2, we theoretically compare this approach with the case where $N = 2m_p$ (refs. 32,33), and we identify a number of key differences; namely, choosing

https://doi.org/10.1038/s41566-023-01326-6

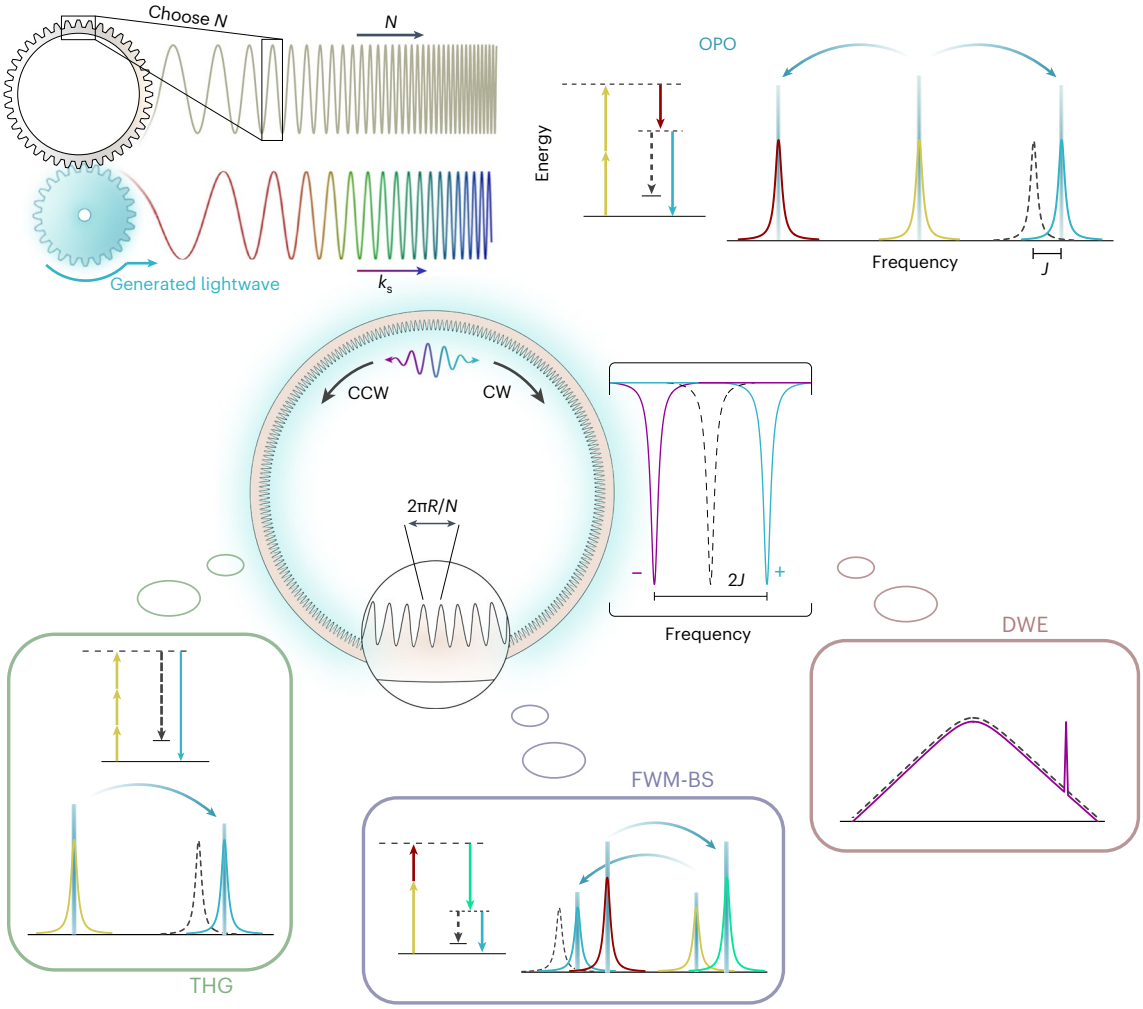

Fig. 1 | Conceptual depictions of wavenumber-selective nonlinear wavelength conversion in Kerr photonic crystal microresonators. Spatial modulation of the microresonator inner sidewall (pictured centre) with a grating period $2\pi R/N$, where N is an integer, coherently couples CW and CCW travelling-wave modes with the azimuthal mode number m_s ($= N/2$) and creates two supermodes, denoted '+' and '−', with frequency separation $2J$, where J is proportional to the sidewall modulation amplitude. We link the spatial frequency of sidewall modulation, N, to the wavenumber, $k_s = N/2R$, of an output wave that is generated via nonlinear wavelength conversion. Hence, the photonic crystal resonator functions like a gear, as illustrated in the top left, to accurately control the wavelengths produced by a given device. Bottom: in resonators with normal GVD, FWM cannot occur between travelling-wave modes due to energy non-conservation (see the energy level diagrams), but frequency matching can be realized using one of the supermodes. This enables, for example, OPO, THG and FWM-BS in microresonators with purely normal GVD, and DWE in microresonators with purely anomalous GVD that support soliton microcombs.

$N = 2m_s$ improves the robustness, wavelength accuracy and tunability of the μOPO.

Importantly, coherent coupling in photonic crystal resonators can facilitate other FWM processes, as illustrated in Fig. 1. Specifically, we explore THG, FWM-BS and DWE, all of which involve wide spectral gaps between their constituent wavelengths and thus exhibit $\Delta\nu$ spectra that are difficult to control exclusively via the cross-sectional geometry of the microresonator. In each case, we can re-define $\Delta\nu$ according to equation (1) (see Supplementary Section I) and use coherent coupling to restore energy conservation by balancing $\Delta\nu_{CW}$ with J. In Fig. 1, the energy diagrams and optical spectra show how shifting the frequency of one mode can promote THG and FWM-BS. The DWE process merits special elaboration. Bright soliton microcombs operate in a regime of anomalous GVD, but certain wavelengths with normal GVD can exhibit local power enhancements (that is, DWE)[24,37]. The DWE phenomenon is useful to aid self-referencing, but the wavelengths of the dispersive waves are difficult to control due to their reliance on higher-order GVD. We envision using wavenumber-selective coherent coupling to dictate the m values of the dispersive waves. Because of the underlying anomalous GVD, the dispersive waves will be resonant with the '−' supermode. This scheme could operate without tailoring higher-order GVD and deterministically select harmonic wavelengths for self-referencing, thus augmenting microcombs spectrally tailored with Fourier synthesis[35].

To prove our ideas, we analyse THG, FWM-BS and DWE in resonators with either purely normal (for THG and FWM-BS) or purely anomalous (for DWE) GVD by including coherent coupling in the simulations of those systems. We reserve μOPO simulations for the next section, where we aim to verify our model with experiments. We use a set of coupled-mode equations to simulate THG and a pair of coupled LLEs to simulate FWM-BS and DWE (for details, see Supplementary Section I). Importantly, we include the coherent coupling explicitly in our models; that is, we do not manually insert frequency shifts into the GVD, since this would not account for the hybridization of the CW/CCW modes. We define the mode spectra and perform simulations in the CW/CCW basis. To include coherent coupling, we allow one CW mode to exchange energy with its CCW counterpart at a coupling rate J that is continuously tunable. In Fig. 2, we present simulated optical spectra for THG,

https://doi.org/10.1038/s41566-023-01326-6

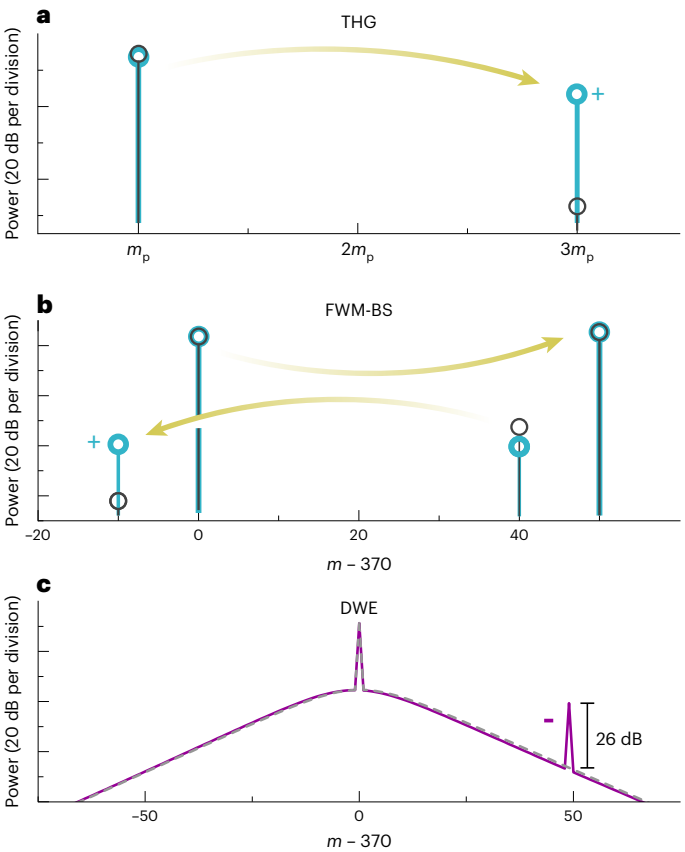

Fig. 2 | Simulations of nonlinear wavelength conversion in Kerr photonic crystal microresonators. The m values designated for coherent coupling are marked by a blue '+' or a purple '−', depending on which supermode is utilized. **a**, Simulated THG spectrum, both with (blue) and without (grey) photonic crystal-mediated coherent coupling (J). The simulation parameters are $\Delta\nu_{CW} = 12.5$ GHz, $J = 12.425$ GHz (blue data only) and $P_{in} = 250$ μW. **b**, Simulated FWM-BS spectrum, both with (blue) and without (grey) coherent coupling. The simulation parameters are $D_2/2\pi = -25$ MHz per mode (which corresponds to $\Delta\nu_{CW} = 12.5$ GHz), $J = 12.6$ GHz (blue data only) and $P_{in} = 5$ mW for both pump lasers. **c**, Simulated Kerr-microcomb spectrum with (purple) and without (dashed grey) coherent coupling. Coherent coupling is used for DWE, to increase the power of a single microcomb tone by 26 dB. The simulation parameters are $D_2/2\pi = 10$ MHz per mode, $J = 13.75$ GHz (purple data only) and $P_{in} = 15$ mW. Higher-order nonlinear effects such as Raman scattering and self-steepening are neglected. Definitions of $\Delta\nu$ for THG and FWM-BS are given in Supplementary Section I.

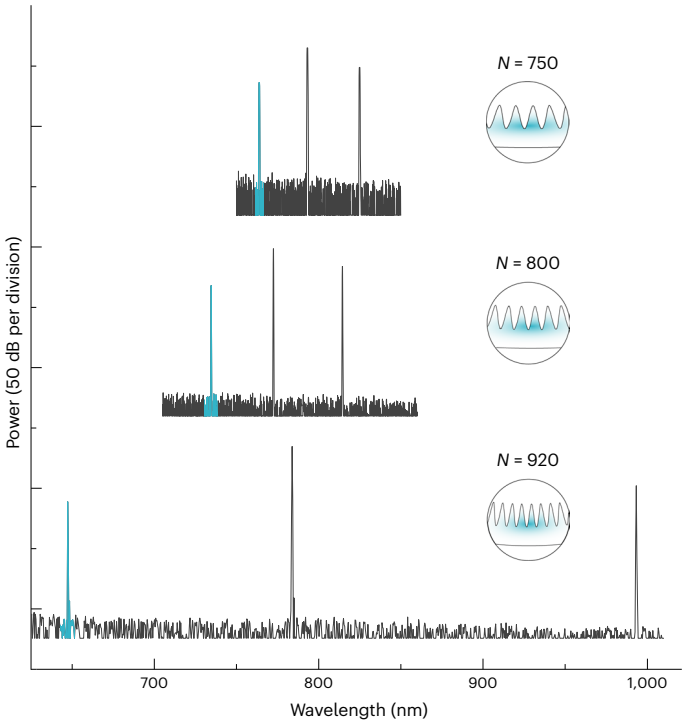

Fig. 3 | Wavenumber-selective μOPOs in Kerr photonic crystal microresonators. Optical spectra generated in three μOPO devices. From top to bottom, $N = 750$, 800 and 920 and $A_{mod} = 5$, 10 and 25 nm, respectively. In each spectrum, the line corresponding to the signal wave is coloured blue, and the signal mode number $m_s = N/2$. Each device exhibits normal GVD at the pump, signal and idler wavelengths.

FWM-BS and DWE. The grey data correspond to simulations with $J = 0$, and the blue or purple data (when utilizing the '+' or '−' supermodes, respectively) correspond to simulations where J is tuned to maximize the signal (or dispersive wave) power.

In our simulations, we assign to all modes a (critically coupled) loaded linewidth $\kappa/2\pi = 500$ MHz. In the THG simulations, we set $\Delta\nu_{CW} = 12.5$ GHz and $P_{in} = 250$ μW, where P_{in} is the pump power. This P_{in} value efficiently drives THG but is below the saturation power (see Supplementary Fig. 1). We apply coherent coupling to the third-harmonic mode. When $J = 0$, the third-harmonic power $P_{3H} \approx 2.7$ nW. We find that $J = 12.425$ GHz maximizes P_{3H}, in accordance with equation (4), increasing it to $P_{3H} \approx 3$ μW, as shown in Fig. 2a.

To model FWM-BS, we simulate a microresonator pumped by two separate pump lasers resonant with modes $m = 370$ and $m = 420$. For both lasers, $P_{in} = 5$ mW. A low-power input seed, resonant with mode $m = 410$, is also injected into the resonator. FWM-BS converts the input seed photons to output signal photons resonant with $m = 360$. We set $D_2/2\pi = -25$ MHz per mode, where D_2 is the second-order term in a Taylor series expression of the integrated dispersion, $D_{int} = \nu_\mu - (\nu_0 + \mu \times \mathrm{FSR})$. This D_2 value corresponds to $\Delta\nu_{CW} = 12.5$ GHz. We apply coherent coupling to the signal mode. When $J = 0$, virtually no seed photons are converted. When $J = 12.6$ GHz, ~25% of input photons are converted to wavelength-shifted output photons, as shown in Fig. 2b. Notably, Liu et al. recently proposed a dispersion engineering approach to FWM-BS that is also based on coherent coupling between CW/CCW modes[38].

To simulate DWE, we set $D_2/2\pi = 10$ MHz per mode and apply coherent coupling to the $m = 419$ mode. A laser, resonant with mode $m = 370$, pumps the resonator with $P_{in} = 15$ mW. When $J = 0$, the microcomb spectrum exhibits a smooth sech^2 profile with no DWEs. When $J = 13.75$ GHz, we observe a 26 dB power enhancement at the targeted mode, as shown in Fig. 2c. In Supplementary Section I, we characterize our simulations in more detail. Remarkably, our modelling captures wavelength conversion into the supermodes, thus illustrating the applicability of our scheme to a variety of Kerr-nonlinear processes.

To validate the main elements of our approach in experiments, we choose an additional Kerr-nonlinear process, that of degenerately pumped μOPO. In processes such as THG and FWM-BS, the potential output wavelength is known a priori from the input wavelengths, with the efficiency of conversion depending on $\Delta\nu$ (as well as other parameters not dependent on the phase- and frequency-matching strategy, namely, resonator–waveguide coupling[16]). By contrast, the μOPO output wavelengths are not determined solely by the input wavelengths, but can vary widely depending on GVD. Therefore, μOPOs provide an ideal experimental test of wavenumber-selective FWM.

To this end, we perform experiments that demonstrate a priori control over m_s in μOPO devices with $N = 2m_s$. In Fig. 3 we present optical spectra generated in three different photonic crystal microresonators with RW′ modulations parameterized by $N = 750$, 800 and 920 and $A_{mod} = 5$, 10 and 25 nm, respectively. In each device, A_{mod} is

https://doi.org/10.1038/s41566-023-01326-6

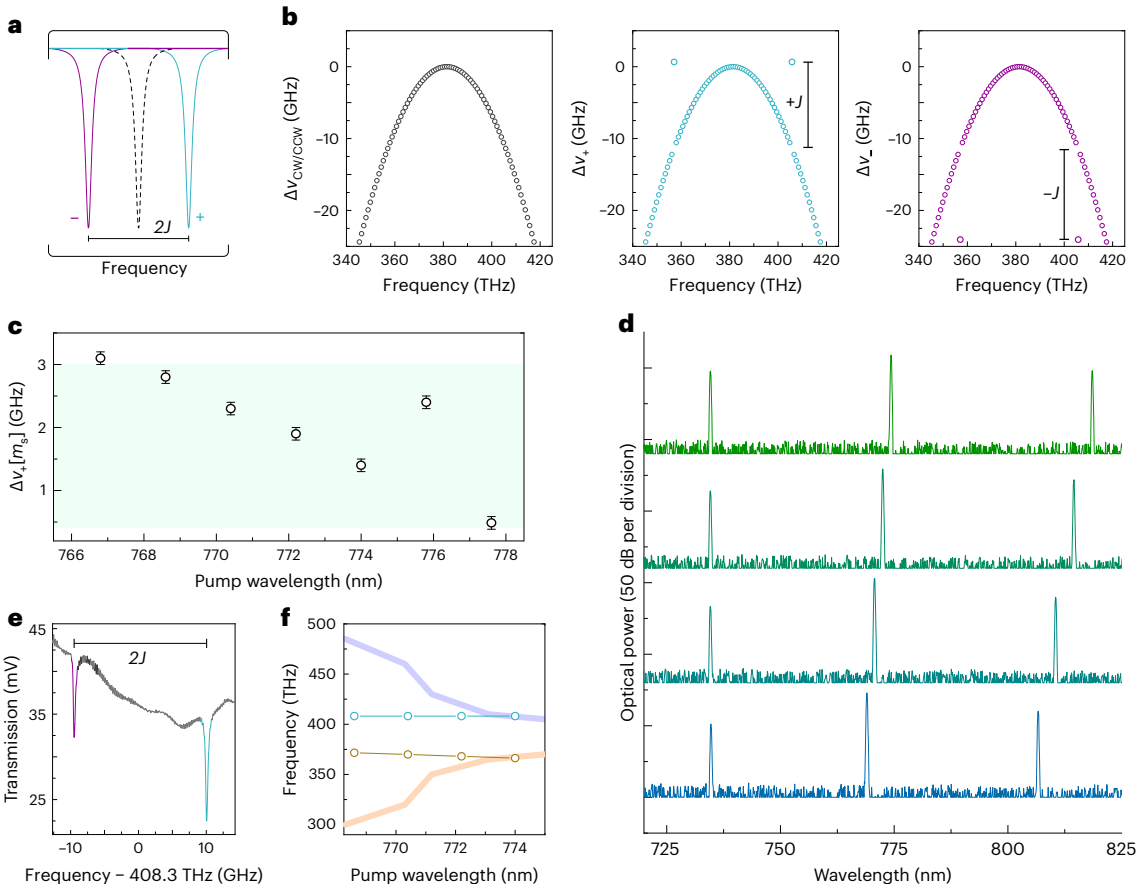

Fig. 4 | Optical parametric oscillation using selective splitting in undulated microrings (OPOSSUM). a, Conceptual transmission spectrum illustrating the frequency splitting of a travelling-wave mode (grey dashed line) into two standing-wave supermodes with frequency separation $2J$. **b**, Simulated $\Delta\nu$ spectra of an OPOSSUM device in the CW/CCW basis (left), the '+' basis (centre) and the '−' basis (right). In the '+' basis, a single mode pair is frequency-matched to enable FWM, and normal GVD mismatches all other mode pairs. **c**, Plot of $\Delta\nu_+$ versus pump wavelength for an OPOSSUM device with $R = 25$ µm, RW = 925 nm, $H = 600$ nm and $N = 800$. Vertical error bars correspond to the range in $\Delta\nu_+$ values obtained when the measurement is repeated ten times. The pale green stripe indicates $\Delta\nu_+$ values conducive to OPO. **d**, Optical spectra obtained from pumping four different modes (with wavelengths between 768 nm and 774 nm) in the OPOSSUM device. **e**, Transmission spectrum of the same device. **f**, OPOSSUM signal (blue circles) and idler (gold circles) frequencies versus the pump wavelength. The pale stripes show the same data, taken from ref. 9, for a device that relies on higher-order GVD engineering for frequency matching.

chosen to balance the underlying normal GVD (in the next section, we explain our design process in more detail). We pump a fundamental transverse-electric (TE0) resonator mode near 780 nm and we observe one of two outcomes: a µOPO with $m_s = N/2$ when J compensates for $\Delta\nu_{CW}$ (that is, the three spectra in Fig. 3); or a CW state (that is, no wavelength conversion; data not shown in Fig. 3) preserved by normal GVD and an incommensurate balance of $\Delta\nu_{CW}$ and J. We confirm the m_s values from mode transmission spectroscopy, and we measure (simulate) signal wavelengths of 763.5 nm (761.5 nm), 735.0 nm (735.8 nm) and 648.0 nm (649.9 nm). This binary distribution of measurement outcomes affirms the protected nature of wavelength conversion in our experiments.

OPO using selective splitting in undulated microresonators (OPOSSUM)

We now explain our procedures for designing photonic crystal microresonators and testing them post-fabrication (for details about the fabrication process, see Methods). We refer to the µOPO mechanism as OPOSSUM, which stands for optical parametric oscillation using selective splitting in undulated microresonators. To start, we reiterate the impact of wavenumber-selective coherent coupling on the resonator mode spectrum: CW and CCW modes with $m = N/2$ hybridize into two supermodes with frequency separation $2J$, as illustrated in Fig. 4a. Hence, OPOSSUM devices exhibit three $\Delta\nu$ spectra, denoted $\Delta\nu_{CW/CCW}$, $\Delta\nu_+$ and $\Delta\nu_-$, depending on the basis used. To choose values for RW, N and A_{mod} (the SiN thickness H is fixed by our current stock of SiN and $R = 25$ µm), we simulate mode spectra using the finite-element method for devices without RW′ modulation. We calculate $\Delta\nu_{CW}$ according to equation (3) and choose an RW value that exhibits broadband normal GVD. Then, we identify a target signal wavelength (for example, 760 nm, 735 nm or 650 nm for the three devices related to Fig. 3b) and choose N accordingly. To select A_{mod}, we fabricate a set of devices with variations in RW, A_{mod} and N, and we measure the frequency splittings to calibrate $J(N, \mathrm{RW}, A_{mod})$. Using our calibrations, we set A_{mod} for a particular device to balance $\Delta\nu_{CW}$. Figure 4b depicts the simulated $\Delta\nu_{CW/CCW}$, $\Delta\nu_+$ and $\Delta\nu_-$ spectra for a device with RW = 925 nm, $H = 600$ nm and $N = 800$. Notably, the $\Delta\nu_+$ spectrum is discontinuous at the signal and idler frequencies, where $\Delta\nu_+ = \Delta\nu_{CW} + J$ (note that, even though coherent coupling is only applied to the signal mode, the $\Delta\nu_+$ values are shifted equally for signal and idler modes because, according to equation (3), $\Delta\nu_+(\mu) = \Delta\nu_+(-\mu)$). This suggests that OPOSSUM suppresses FWM involving modes other than the targeted signal and idler, since at these frequencies the resonator exhibits strong normal dispersion.

Next, we perform experiments to characterize OPOSSUM. We fabricate the OPOSSUM device simulated in Fig. 4b and measure the TE0 mode wavelengths to calculate $\Delta\nu_+[m_s]$ (that is, the value of $\Delta\nu_+$ at

https://doi.org/10.1038/s41566-023-01326-6

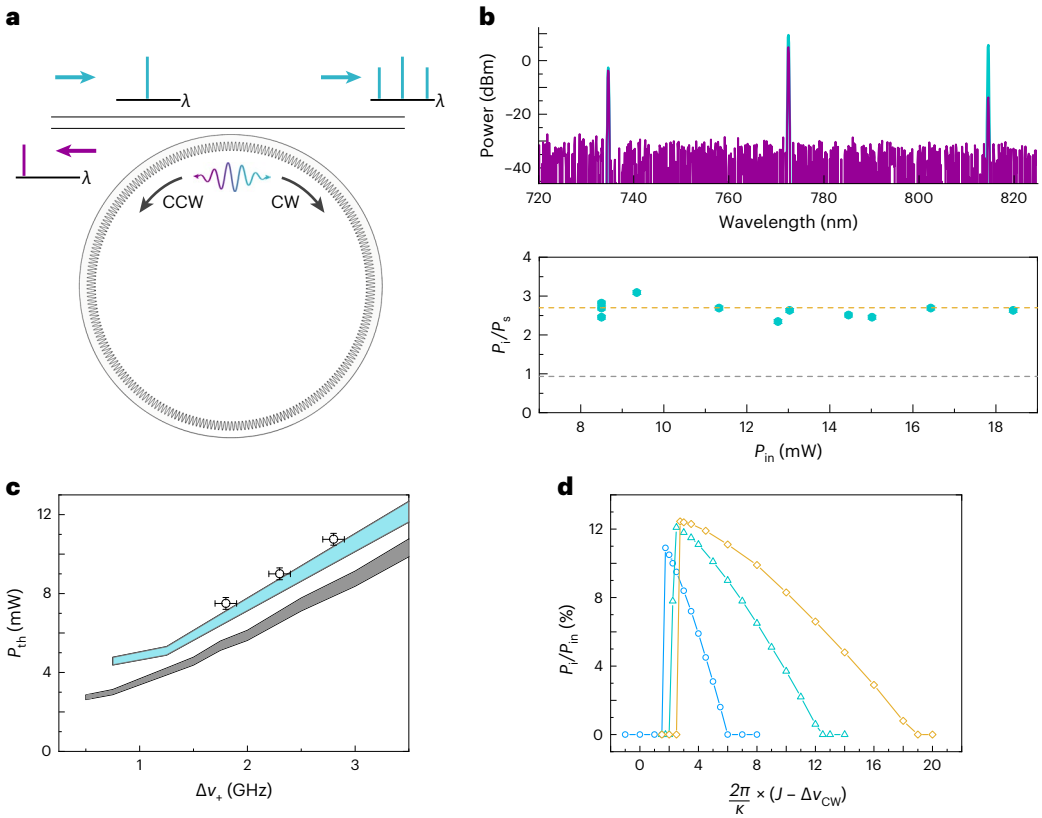

Fig. 5 | Modelling OPOSSUM with the LLE. a, Illustration of OPOSSUM spectra. Owing to CW/CCW coupling, some fraction of the signal photons is outcoupled counterpropagating the injected pump. λ, wavelength. **b**, Top: OPOSSUM spectrum calibrated to indicate the on-chip power. Blue (purple) data correspond to transmitted (reflected) light. Bottom: measured ratio (P_i/P_s) of transmitted idler power (P_i) to transmitted signal power (P_s) versus P_{in}. The orange (grey) dashed line is calculated from LLE simulations that include (do not include) CW/CCW coupling. **c**, Measured threshold power (P_{th}) versus $\Delta\nu_+$. Vertical error bars denote uncertainties in optical losses between the input and output fibres, calculated as one standard deviation in loss measurements repeated ten times. Horizontal error bars correspond to the range in $\Delta\nu_+$ values obtained when the measurement is repeated ten times, and they are centred at the mean. The blue and grey stripes are calculated from LLE simulations that include (blue) and do not include (grey) CW/CCW coupling. The finite thicknesses of the theory curves correspond to uncertainties in the value of the Kerr nonlinear coefficient. **d**, Simulated idler conversion efficiency (P_i/P_{in}) versus normalized J for P_{in} = 10 mW (blue circles), P_{in} = 20 mW (green triangles) and P_{in} = 30 mW (gold diamonds).

the targeted signal mode). Importantly, $\Delta\nu_+[m_s]$ depends on m_p; hence, tuning the pump wavelength can correct for fabrication uncertainties and, more generally, ensure reliable operation. To concretize this idea, we measure $\Delta\nu_+[m_s]$ versus the pump wavelength, as shown in Fig. 4c. We find that $\Delta\nu_+[m_s]$ decreases with increasing pump wavelength, with an exception near 776 nm, where we observe mode crossings at the pump and idler wavelengths. In principle, we can generate a μOPO using any pump mode such that $\Delta\nu_+[m_s] > 0$, provided that P_{in} is large enough to induce compensating nonlinear mode frequency shifts[25]. Realistically, however, we prefer $\Delta\nu_+[m_s]$ to be <3 GHz. Greater $\Delta\nu_+$ values require $P_{in} > 50$ mW to produce appreciable signal and idler powers; at this level, absorption-induced temperature shifts can destabilize the μOPO. At the same time, we require $\Delta\nu_+[m_s] > \kappa/4\pi$. In our OPOSSUM devices, we measure typical loaded quality factor (Q) values between 5×10^5 and 7×10^5 (with some dependence on wavelength), so the four pump modes spanning wavelengths 768–774 nm satisfy these requirements, as indicated by the pale stripe in Fig. 4c. Indeed, pumping any of these modes results in a μOPO. We record the optical spectra and present them in Fig. 4d. As expected, m_s is fixed—its value is protected by the wavenumber-selective coherent coupling, with an example transmission spectrum shown in Fig. 4e. In Fig. 4f, we present measurements of the signal and idler frequencies (ν_s and ν_i, respectively) versus the pump wavelength. We overlay similar data (pale stripes), taken from ref. 9, for a μOPO system that relies on higher-order GVD, where the dispersion sensitivity is apparent from the large shifts in ν_s (and ν_i) when tuning the pump laser between adjacent pump modes (that is, with consecutive m_p values). By comparison, OPOSSUM is a robust mechanism for targeting specific wavelengths. In Supplementary Section II, we analyse the microresonator GVD and its connection to such robustness.

Next, we investigate the OPOSSUM efficiency and threshold behaviour. To model OPOSSUM, we simulate a pair of coupled LLEs that describe the intraresonator evolution of the CW and CCW fields. We are especially interested in connections between our experimental parameters and the power generated in the signal and idler waves. Intuitively, we expect the signal wave, which occupies the '+' supermode, to propagate in both CW and CCW directions; hence, we should detect some signal light at the input (reflection) port of a device, as shown in Fig. 5a. In simulations, we observe approximately 20% more signal power in the reflection port than the transmission port. This distribution is approximately independent of P_{in} and $\Delta\nu_+$. In experiments, we measure an approximately equal distribution of signal power to the two ports. The top panel of Fig. 4 shows the optical spectra calibrated to estimate the on-chip power levels at the transmission (blue) and reflection (purple) ports of the OPOSSUM device characterized in Fig. 5a. The presence of reflected pump and idler light is due to Fresnel reflections at the waveguide facets, but such light is still strongly suppressed relative to the transmission port (for example, ~20 dB for the idler). Ultimately, large optical losses that occur during propagation from the reflection port to the optical spectrum analyser prevent

https://doi.org/10.1038/s41566-023-01326-6

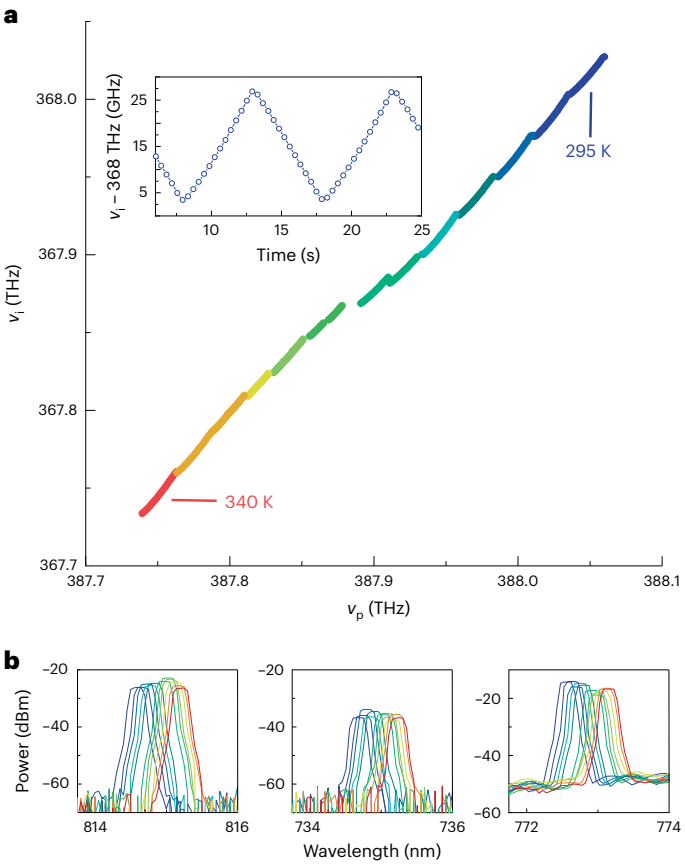

Fig. 6 | Exploring wavelength tunability in OPOSSUM. a, Wavemeter measurement of ν_i versus ν_p at 11 different temperatures (corresponding to the 11 different colours). The temperature is used to tune ν_i coarsely, while controlling ν_p enables fine tuning. Inset: wavemeter measurement of ν_i versus time during a ν_p sweep. **b**, Optical spectra zoomed into the idler (left), signal (middle) and pump (right) bands at each temperature. These measurements show that output power is maintained across the tuning range.

a precise measurement of the signal power distribution. A more precise comparison can be made between the transmitted powers of the signal and idler waves, denoted P_s and P_i, respectively. Specifically, we calculate P_i/P_s versus P_{in} and indicate our measurements with blue data points in the bottom panel of Fig. 5b. Our measurements agree with simulation results shown by the orange dashed line. Notably, we find that P_i/P_s does not depend on P_{in}. Moreover, the unequal distribution of photons between signal and idler waves is unique within the Kerr microring resonator platform—previous (non-OPOSSUM) μOPO systems exhibited an equal distribution of photons ensured by the symmetry of degenerate FWM[25]. In OPOSSUM, this symmetry is broken by CW/CCW coupling. Finally, we note that signal light propagating in the CW/CCW directions can be coherently re-combined outside the resonator to increase P_s.

To characterize OPOSSUM further, we measure the threshold power for parametric oscillation (P_{th}), which is another important parameter of μOPO systems. Conveniently, we can measure P_{th} versus $\Delta\nu_+$ by choosing different pump modes, as shown in Fig. 5c. The P_{th} values predicted from our model are shown by the blue stripe, and the P_{th} values predicted from a crude model (consisting of a single LLE wherein we shift the signal mode frequency by J) are shown by the grey stripe. Our measurements support the validity of our model. Next, we explore the robustness of OPOSSUM with respect to variation in J. Such an investigation conveys the design tolerance of OPOSSUM, that is, the allowable errors in device geometry that can arise from fabrication uncertainties. Specifically, we simulate OPOSSUM and calculate the conversion efficiency (P_i/P_{in}) versus J for P_{in} = 10, 20 and 30 mW, as shown in Fig. 5d. We find that the maximum conversion efficiency is 12.5% for a critically coupled resonator, which is the same result derived recently for other μOPO systems (the maximum conversion efficiency can be increased by overcoupling the resonator, at the cost of greater P_{th}). Moreover, the range of J values that supports a given efficiency increases with P_{in}. For instance, to realize $P_i \geq 2$ mW with P_{in} = 20 mW, we find $22 \leq 2J \leq 25$ GHz, where $\kappa/2\pi$ = 500 MHz and $\Delta\nu_{CW}$ = 10 GHz. For the device characterized in Fig. 5b,c, this corresponds roughly to $11 \leq A_{mod} \leq 12.5$ nm. The possibility of increasing design tolerances using, for example, temperature tuning, requires further study.

Finally, we explore the wavelength tunability of OPOSSUM using the same device characterized in Figs. 4 and 5. Such tunability is of practical importance to nonlinear wavelength converters aiming for, for example, specific atomic transitions. In our experiments, we sweep the pump frequency ν_p by ~25 GHz in 5 s while sustaining a μOPO, and we observe the resulting changes in ν_i using a wavemeter (ν_s can be inferred from ν_i and ν_p using equation (1)). An example of these data is shown in the inset to Fig. 6a. We find that $\frac{d\nu_i}{d\nu_p} \approx 1$. To extend the wavelength access of our OPOSSUM device, we increase its temperature T according to $\frac{d\nu_0}{dT} \approx -4$ GHz K^{-1} and repeat the ν_p sweep while recording ν_i. Figure 6a shows our results from repeating this measurement at 11 different temperatures (corresponding to the 11 different colours in Fig. 6), from $T \approx 295$–340 K, chosen to access all frequencies between $367.73 \leq \nu_i \leq 368.02$ THz. (At some temperatures, we found that ν_p could be swept >25 GHz while sustaining the μOPO. This is why some colours comprise more frequencies than others in Fig. 6a.) At each temperature, we record the optical spectrum, as shown in Fig. 6b where we have magnified the idler, signal and pump bands in the left, middle and right panels, respectively. Importantly, the μOPO output power is maintained across the entire tuning range. Moreover, the nearly 300 GHz of tuning reported here was only limited by instabilities in our setup at the higher temperatures. Given such stability, we expect that greater tuning ranges, possibly exceeding the FSR, are attainable. Our measurements suggest that a suitable choice of N, combined with continuous tunability, gives deterministic wavelength control with high accuracy.

Discussion

Importantly, through the OPOSSUM mechanism we achieve 99.7% wavelength accuracy without iterating fabrication runs (that is, to target specific wavelengths, we identify N values based only on our finite-element simulations, with little guidance from previous measurements). Moreover, temperature tuning beyond the ~50 K range that we can achieve in experiments will compensate for wavelength inaccuracies. In cases where $\Delta\nu_+$ depends on T, one can leverage the relationship between $\Delta\nu_+$ and m_p. For instance, if T must be adjusted so much that a μOPO is destabilized when pumping mode m_p, then switching to $m_p \pm 1$ (depending on whether T has been increased or decreased) will restore frequency matching.

In conclusion, we have shown that coherent coupling in photonic crystal resonators can facilitate FWM-based nonlinear wavelength conversion without higher-order GVD. We theoretically investigated four $\chi^{(3)}$ processes within such resonators: FWM-BS, THG, DWEs in microcombs and OPO. In all cases we found that large efficiencies could be achieved for a specific targeted mode, establishing a basis for wavelength accuracy in Kerr-nonlinear photonics, and future optimization of the method should lead to even larger efficiencies than we report here. Moreover, we explored how the photonic crystal structure gives excellent control over generated wavelengths while protecting the FWM process from unwanted nonlinear couplings. To affirm the simulation results, we experimentally focused on the specific case of

OPO, which is typically distinguished by a substantial sensitivity of the output wavelengths to the device geometry and pump wavelength. We generated μOPOs with signal wavenumbers defined by the photonic crystal grating period. We measured the conversion efficiencies and threshold powers for multiple devices, and our measurements agreed with the simulations. Finally, we demonstrated continuous tunability of the μOPO spectrum. Importantly, we expect that coherent coupling can be implemented in resonant $\chi^{(2)}$-nonlinear systems, in addition to the $\chi^{(3)}$ systems discussed here. The devices and methods introduced here will be invaluable to future nanotechnologies that utilize application-tuned and wavelength-accurate nonlinear photonics.

Online content

Any methods, additional references, Nature Portfolio reporting summaries, source data, extended data, supplementary information, acknowledgements, peer review information; details of author contributions and competing interests; and statements of data and code availability are available at https://doi.org/10.1038/s41566-023-01326-6.

References

1. Ludlow, A. D., Boyd, M. M., Ye, J., Peik, E. & Schmidt, P. O. Optical atomic clocks. *Rev. Mod. Phys.* **87**, 637–701 (2015).
2. Bothwell, T. et al. Resolving the gravitational redshift across a millimetre-scale atomic sample. *Nature* **602**, 420–424 (2022).
3. Wehner, S., Elkouss, D. & Hanson, R. Quantum internet: a vision for the road ahead. *Science* **362**, eaam9288 (2018).
4. Elshaari, A. W., Pernice, W., Srinivasan, K., Benson, O. & Zwiller, V. Hybrid integrated quantum photonic circuits. *Nat. Photon.* **14**, 285–298 (2020).
5. Spencer, D. T. et al. An optical-frequency synthesizer using integrated photonics. *Nature* **557**, 81–85 (2018).
6. Newman, Z. L. et al. Architecture for the photonic integration of an optical atomic clock. *Optica* **6**, 680–685 (2019).
7. Riemensberger, J. et al. Massively parallel coherent laser ranging using a soliton microcomb. *Nature* **581**, 164–170 (2020).
8. Gaeta, A. L., Lipson, M. & Kippenberg, T. J. Photonic-chip-based frequency combs. *Nat. Photon.* **13**, 158–169 (2019).
9. Lu, X., Moille, G., Rao, A., Westly, D. A. & Srinivasan, K. On-chip optical parametric oscillation into the visible: generating red, orange, yellow, and green from a near-infrared pump. *Optica* **7**, 1417–1425 (2020).
10. Sayson, N. L. B. et al. Octave-spanning tunable parametric oscillation in crystalline Kerr microresonators. *Nat. Photon.* **13**, 701–706 (2019).
11. Marty, G., Combrié, S., Raineri, F. & De Rossi, A. Photonic crystal optical parametric oscillator. *Nat. Photon.* **15**, 53–58 (2021).
12. Vernon, Z. et al. Scalable squeezed-light source for continuous-variable quantum sampling. *Phys. Rev. Appl.* **12**, 064024 (2019).
13. Dutt, A. et al. On-chip optical squeezing. *Phys. Rev. Appl.* **3**, 044005 (2015).
14. Kues, M. et al. Quantum optical microcombs. *Nat. Photon.* **13**, 170–179 (2019).
15. Lu, X. et al. Chip-integrated visible–telecom entangled photon pair source for quantum communication. *Nat. Phys.* **15**, 373–381 (2019).
16. Li, Q., Davanço, M. & Srinivasan, K. Efficient and low-noise single-photon-level frequency conversion interfaces using silicon nanophotonics. *Nat. Photon.* **10**, 406–414 (2016).
17. Carmon, T. & Vahala, K. J. Visible continuous emission from a silica microphotonic device by third-harmonic generation. *Nat. Phys.* **3**, 430–435 (2007).
18. Surya, J. B., Guo, X., Zou, C.-L. & Tang, H. X. Efficient third-harmonic generation in composite aluminum nitride/silicon nitride microrings. *Optica* **5**, 103–108 (2018).
19. Boyd, R. W. *Nonlinear Optics* (Academic, 2020).
20. Yang, K. Y. et al. Broadband dispersion-engineered microresonator on a chip. *Nat. Photon.* **10**, 316–320 (2016).
21. Okawachi, Y. et al. Bandwidth shaping of microresonator-based frequency combs via dispersion engineering. *Opt. Lett.* **39**, 3535–3538 (2014).
22. Lu, X. et al. Efficient telecom-to-visible spectral translation through ultralow power nonlinear nanophotonics. *Nat. Photon.* **13**, 593–601 (2019).
23. Yu, S.-P. et al. Tuning Kerr-soliton frequency combs to atomic resonances. *Phys. Rev. Appl.* **11**, 044017 (2019).
24. Briles, T. C. et al. Interlocking Kerr-microresonator frequency combs for microwave to optical synthesis. *Opt. Lett.* **43**, 2933–2936 (2018).
25. Stone, J. R., Moille, G., Lu, X. & Srinivasan, K. Conversion efficiency in Kerr-microresonator optical parametric oscillators: from three modes to many modes. *Phys. Rev. Appl.* **17**, 024038 (2022).
26. Zhang, Y. et al. Squeezed light from a nanophotonic molecule. *Nat. Commun.* **12**, 2233 (2021).
27. Tang, Y., Gong, Z., Liu, X. & Tang, H. X. Widely separated optical Kerr parametric oscillation in AlN microrings. *Opt. Lett.* **45**, 1124–1127 (2020).
28. Urbonas, D., Balčytis, A., Vaškevičius, K., Gabalis, M. & Petruškevičius, R. Air and dielectric bands photonic crystal microringresonator for refractive index sensing. *Opt. Lett.* **41**, 3655–3658 (2016).
29. Lo, S. M. et al. Photonic crystal microring resonator for label-free biosensing. *Opt. Express* **25**, 7046–7054 (2017).
30. Lu, X., McClung, A. & Srinivasan, K. High-Q slow light and its localization in a photonic crystal microring. *Nat. Photon.* **16**, 66–71 (2022).
31. Yu, S.-P. et al. Spontaneous pulse formation in edgeless photonic crystal resonators. *Nat. Photon.* **15**, 461–467 (2021).
32. Lu, X., Chanana, A., Zhou, F., Davanco, M. & Srinivasan, K. Kerr optical parametric oscillation in a photonic crystal microring for accessing the infrared. *Opt. Lett.* **47**, 3331–3334 (2022).
33. Black, J. A. et al. Optical-parametric oscillation in photonic-crystal ring resonators. *Optica* **9**, 1183–1189 (2022).
34. Lu, X., Rao, A., Moille, G., Westly, D. A. & Srinivasan, K. Universal frequency engineering tool for microcavity nonlinear optics: multiple selective mode splitting of whispering-gallery resonances. *Photon. Res.* **8**, 1676–1686 (2020).
35. Moille, G., Lu, X., Stone, J., Westly, D. & Srinivasan, K. Fourier synthesis dispersion engineering of photonic crystal microrings for broadband frequency combs. *Commun. Phys.* **6**, 144 (2023).
36. Lucas, E., Yu, S.-P., Briles, T. C., Carlson, D. R. & Papp, S. B. Tailoring microcombs with inverse-designed, meta-dispersion microresonators. *Nat. Photon.* **17**, 943–950 (2023).
37. Moille, G., Westly, D., Orji, N. G. & Srinivasan, K. Tailoring broadband Kerr soliton microcombs via post-fabrication tuning of the geometric dispersion. *Appl. Phys. Lett.* **119**, 121103 (2021).
38. Liu, J. et al. Tunable frequency matching for efficient four-wave-mixing Bragg scattering in microrings. *Opt. Express* **29**, 36038–36047 (2021).

Methods

Fabrication methods

We deposit stoichiometric SiN via low-pressure chemical vapour deposition on top of a 3-µm-thick layer of SiO_2 on a 100-mm-diameter Si wafer. We fit ellipsometer measurements of the wavelength-dependent SiN refractive index and layer thicknesses to an extended Sellmeier model. The device pattern is created in positive-tone resist using electron-beam lithography and then transferred to SiN via reactive-ion etching using CF_4/CHF_3 chemistry. After cleaning the devices, we anneal them for 4 h at 1,100 °C in N_2. Next, we perform a liftoff of SiO_2 so that the resonator has an air top cladding for dispersion purposes while the perimeter of the chip is SiO_2-clad for better coupling to lensed optical fibres. The facets of the chip are then polished for lensed-fibre coupling. After polishing, the chip is annealed again.

Measurement of $\Delta\nu$

To measure $\Delta\nu$ in our devices, we use laser transmission spectroscopy to measure the resonance frequencies of TE0 resonator modes in the wavelength regions of interest, and $\Delta\nu$ is calculated according to equation (3). We use a tunable, continuous-wave titanium:sapphire (TiS) laser to perform the spectroscopy. We tune the TiS laser to a TE0 resonator mode, minimize the transmission and record the TiS frequency using a wavemeter. The TiS laser power is kept at <1 µW to avoid thermo-optic mode-frequency shifts.

Data availability

The datasets generated during and/or analysed during the current study are available from the corresponding authors upon reasonable request.

Code availability

The programs used to simulate the coupled-mode and Lugiato–Lefever equations are available from the corresponding authors upon reasonable request.

Acknowledgements

We thank E. Perez and M. Chojnacky for providing useful feedback during the preparation of the paper. We acknowledge funding support from the the DARPA LUMOS and NIST-on-a-chip programmes.

Author contributions

J.R.S. envisioned and performed the experiments and analysed the data. X.L. fabricated the devices, contributed experimental ideas and assisted with device design. G.M. assisted with device design and helped to analyse the data. D.W. fabricated the devices, T.R. helped to characterize the devices and K.S. analysed the data and consulted on the experiments.

Competing interests

NIST/UMD have filed patent applications, with J.R.S., K.S. and X.L. listed as the inventors. The other authors declare no competing interests.

Additional information

Supplementary information The online version contains supplementary material available at https://doi.org/10.1038/s41566-023-01326-6.

Correspondence and requests for materials should be addressed to Jordan R. Stone or Kartik Srinivasan.

Peer review information *Nature Photonics* thanks Alfredo de Rossi, Dawn Tan and the other, anonymous, reviewer(s) for their contribution to the peer review of this work.